

Very-Low-Frequency Electromagnetic Field Detector With Data Acquisition

Saba A. Hanna, *Member, IEEE*, Yuichi Motai, *Member, IEEE*,
Walter J. Varhue, and Stephen Titcomb, *Senior Member, IEEE*

Abstract—Naturally occurring electromagnetic oscillating fields in the very-low-frequency (VLF) range of the spectrum, i.e., from 1 to 200 kHz, are weak and difficult to detect under normal conditions. These naturally occurring VLF electromagnetic events are observed during thunderstorms, in certain mountain winds, and during earthquakes. On the other hand, man-made VLF electromagnetic fields are stronger and have been suspected of causing negative health effects. Typical sources of these VLF emissions include television sets, video display terminals (VDTs), certain medical devices, some radio stations, and the ground-wave emergency network (GWEN) used for military communications. This paper describes the development of a triaxial “VLF gaussmeter,” which can be made portable. This electronic system can be used to monitor VLF electromagnetic radiation in residential and occupational environments. The “VLF gaussmeter” is based on a microcontroller with a built-in 10-bit A/D converter and has been designed to measure the magnetic flux density and frequency across the wide VLF bandwidth (BW). A digitized resolution of 0.2 mG is used for the 0–200-mG range, and 2-mG resolution is used for the range of 2–2000 mG. The meter has been designed to include the following features: 1) automatic or manual range selection; 2) data logging; 3) single-axis mode; 4) peak hold; 5) RS-232 communication port; and 6) analog recorder output.

Index Terms—Biological effects, electromagnetic field (EMF), gaussmeter, very low frequency (VLF).

I. INTRODUCTION

THE POTENTIAL deleterious health effects of electromagnetic field (EMF) radiation [1], [2] is a continuing concern of scientists and engineers. Our environment has always contained this type of radiation as a result of solar activity, meteorological changes, and biosphere activity. EMFs today are also generated by man-made systems such as high-power transmission lines, electrical equipment, radiolocation stations, and communication systems. EMF radiation has been potentially linked to the disruption of many biological systems; some examples include the following: 1) childhood leukemia [3], 2) calcium transport across cell membranes [4], 3) enhanced DNA synthesis [5], 4) brain-wave entrainment [6], 5) inhibition

of lymphocyte activity, 6) chronic stress [7], 7) childhood tumors [8], 8) mechanical vibration of brain tissue [9], and 9) spontaneous abortions [10]. The potential biological effects of extremely low frequency (ELF) and very-low-frequency (VLF) electromagnetic radiation necessitate the development of a handheld surveillance meter.

It is proposed to quantify this radiation field with a device that measures the magnetic field component. The measured magnetic field can be any one of the vector components (B_x , B_y , or B_z) or the resultant ($\sqrt{B_x^2 + B_y^2 + B_z^2}$) of periodic magnetic fields. This magnetic field meter, which is described in this paper, has been designed to have a wide dynamic measurement range from 0.2 to 2000 mG (10 mG = 1 μ T), with a wide-bandwidth (BW) frequency response from 1 to 200 kHz. The detection circuit utilizes three orthogonal multi-turn copper loops that respond to time-varying magnetic fields. The field measurements are also made available externally through an RS-232 communication port and an analog recorder output. The challenge is to construct a unique magnetic flux density recording device with high measurement precision and wide BW as a portable standalone meter. Until now, none of the commercially available portable meters with this frequency range have included all of the features listed above.

This paper is organized as follows. Section II discusses some of the related work that has already been done in the areas of ELF and VLF magnetic field measurements. Section III discusses the theory of operation of this device. Section IV describes the operation of the magnetic field meter, including the analog front end, the design approaches, and a SPICE simulation of the analog subsystem [11]; this incorporates integration, filtration, amplification, ac-to-dc conversion, and a comparator for the frequency detection design. Section V covers the digital components and the firmware for the microcontroller design. Sections VI and VII discuss the system architecture, characterization, and calibration of the meter, along with other alternative design approaches.

II. RELATED WORK IN MAGNETIC FLUX MEASUREMENT

Electromagnetic radiation is classified as either nonionizing or ionizing. Nonionizing radiation consists of electromagnetic waves starting in the low end of the UV frequencies [12], i.e., in the 10^{15} -Hz range, and continuing down to 0 Hz. These photons do not have the energy required to break atomic bonds but can still heat matter [13] at frequencies above 100 kHz.

On the other hand, ionizing radiation ($f > 10^{15}$ Hz) consists of photons with sufficient energy to free electrons from atoms.

Manuscript received November 25, 2007; revised April 28, 2008. First published July 15, 2008; current version published December 9, 2008. The Associate Editor coordinating the review process for this paper was Prof. Alessandro Ferrero.

S. A. Hanna is with the Integrity Design and Research Corporation, Essex, VT 05452 USA, and also with the Department of Electrical Engineering, University of Vermont, Burlington, VT 05405 USA (e-mail: saba@integritydesign.com).

Y. Motai, W. J. Varhue, and S. Titcomb are with the Department of Electrical Engineering, University of Vermont, Burlington, VT 05405 USA (e-mail: ymotai@cems.uvm.edu; varhue@cems.uvm.edu; titcomb@cems.uvm.edu).

Color versions of one or more of the figures in this paper are available online at <http://ieeexplore.ieee.org>.

Digital Object Identifier 10.1109/TIM.2008.927191

X-rays, gamma rays, and cosmic rays are included in this category. In general, ionizing radiation is characterized by short wavelengths and high energy.

The nonionizing part of the electromagnetic spectrum can be divided into several ranges: 1) ELF (0–1000 Hz); 2) VLF (1–200 kHz); 3) radio frequency (0.2–300 MHz); 4) microwave (0.3–300 GHz); 5) infrared (0.3–400 THz); 6) visible light (400–800 THz); and 7) low-frequency UV (0.8–1 PHz). The UV spectrum from 1–1000 PHz is classified as ionizing radiation. The classification of the electromagnetic spectrum may vary due to local conventions throughout the world.

Previous papers discussing instruments working in the non-ionizing range of the electromagnetic spectrum have covered magnetic field monitors and sensors operating in a wide frequency range. The portion of the VLF range from 50 to 200 kHz has not been widely covered, despite the importance of this range to modern society.

Previously, the development of a portable dosimeter with a bandpass filter centered at a frequency of 60 Hz was described by Lo *et al.* [14]. In another study, the design of a precision gaussmeter with an ac BW up to 10 kHz was described by Sedgwick *et al.* [15]. This instrument utilized a single-axis Hall element probe that was not sensitive enough to detect fields in the milligauss level and did not have embedded data-logging capabilities.

A stationary system that uses a personal computer to record the magnetic field on a digital scope was described in a paper by Guttman *et al.* [16]. Two different sets of orthogonal magnetic field sensors were used to cover the frequency range from 40 Hz to 500 MHz. Ferrite core inductor coils were used as sensors for the low-frequency magnetic fields from 40 Hz up to 5 kHz, and active loop antennas were used for the high-frequency range from 5 kHz to 500 MHz. The antennas had a maximum sensitivity of 4 V/mG and were flat to above 100 kHz. The antenna response decreased to 1 V/mG at 10 kHz and continued to decrease to a minimum of 0.2 V/mG for frequencies below 1 kHz. This antenna implementation caused a nonlinear response in the VLF range.

Malcovati and Maloberti [17] developed an integrated microsystem for 3-D magnetic field measurements. The system was based on a multichip module that contains three separate channels for the three components of the magnetic field (B_x , B_y , B_z), with a microprocessor and memory devices. The data was stored in a microchip and required downloading to a personal computer for analysis. This system only covered the low-frequency range around 60 Hz.

There is a need to develop an instrument capable of accurately and conveniently measuring the magnetic field intensity in the VLF range from 50 to 200 kHz. The current paper discusses the design and operational performance of such a system.

III. THEORY OF SENSOR DESIGN

A multiturn copper coil is used as a field-sensing element in this detector design. A coil element is well suited for this application since its sensitivity is higher than that of a Hall-effect sensor at frequencies greater than 30 kHz. According to Faraday's law of induction, an electromotive force is generated

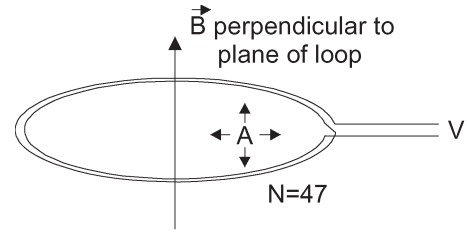


Fig. 1. Air coil loop sensor where the number of turns N is equal to 47 #38 Cu, and the cross-sectional area A is equal to 5.0 cm².

in a closed loop when placed in a time-varying magnetic field. The voltage V_{in} or electromotive force is induced along a coil's length and is proportional to the time rate of change (time derivative) of the magnetic flux [18]

$$V_{in} = -N \left(\frac{d\phi}{dt} \right) \quad (1)$$

where

N number of turns;

ϕ magnetic flux.

Equation (1) can be rewritten as the following for a loop sensor with a fixed diameter d :

$$V_{in} = -\frac{N\pi d^2}{4} \cdot B_0 j\omega e^{j\omega t} \quad (2)$$

where

B_0 amplitude of the magnetic flux density;

ω radian frequency.

Considering only the magnitude for (2)

$$V = |V_{in}| = \frac{N\pi d^2 B_0 \omega}{4} = \frac{N\pi^2 d^2 f}{2} B_0 \quad (3)$$

and solving for N

$$N = \frac{V}{2\pi f B_0 A}. \quad (4)$$

The sensitivity of the detector system can be estimated as a ratio of (V/B_0) with

$$\text{Sensitivity} = \frac{V}{B_0} = 2\pi f N A. \quad (5)$$

A sketch of the induction coil sensor is shown in Fig. 1. A coil of 5 cm² has been chosen for the convenience of use and resolution of the potential measurement. Further, it is desired to use standard electronic hardware, and therefore, a maximum voltage amplitude of 6 V will result from a magnetic flux density of 2000 mG and a frequency of 200 kHz. A design based on these assumptions and goals yields a sensor that contains 47 wire turns using (4).

The detector sensitivity, as predicted in (5), yields 15 μ V/mG and 3.0 mV/mG for f_{min} and f_{max} , respectively. For comparison, a very sensitive Hall sensor with a magnetic flux concentrator has a sensitivity of only 18 μ V/mG for frequencies up to 1 kHz. Above that frequency, the sensitivity will decrease.

The calculated output voltages expected for the coil designed according to (5) with the physical dimension specified above are summarized in Table I, which covers the full operating

TABLE I
EXPECTED OUTPUT VOLTAGES GENERATED BY THE COIL
USING DIFFERENT VALUES OF FREQUENCY
AND MAGNETIC FLUX DENSITY

Frequency (Hz)	Magnetic Flux Density (mG)	Coil Output (V)
1000	0.2	3.00e-06
1000	2000	3.00e-02
200000	0.2	6.00e-04
200000	2000	6.00

range with minimum and maximum values for the frequency and magnetic field strength.

IV. ANALOG SIGNAL PROCESSING

The analog front end of the sensor circuitry associated with each of the three orthogonal coils is represented as a block diagram in Fig. 2. The signal from each coil is filtered by a unity-gain 100-Hz second-order high-pass filter to reject the 60-Hz noise usually found in household and industrial environments. This output signal is then fed into an integrator section that provides a flat frequency response. The output of the integrator is sequentially filtered and amplified by 100-Hz second-order high-pass and 500-kHz low-pass filters to ensure that only the desired signals are fed to the high-gain amplifier stage. A variable-gain amplifier is used to allow measurements over multiple ranges. A gain of 50 is used for the 200-mG range, and a gain of 5 is used for the 2000-mG range. The signal is finally fed to an ac-to-dc converter, where the dc output is compatible with the 0–5-V range of the analog-to-digital converter (ADC). The same signal is also fed to a comparator to generate a digital signal (0 V or 5 V) compatible with the frequency counter. A more complete discussion of the individual components that make up the analog front-end design in Fig. 2 follows in Sections IV-A–E.

A. AC Integrator Design

It can be seen from (5) that the coil output voltage is proportional to both the field magnitude and the signal frequency. The design objective of the meter is to measure only the magnitude of the magnetic field, thus removing any frequency dependence in the measurement. The output of the ac integrator shown in Fig. 3 is inversely proportional to the input frequency, and therefore, it can be used to cancel the frequency dependence from the input signal.

The ac integrator [19] shown in Fig. 3 is placed in the analog sensor circuit immediately following the high-pass noise filter, as shown in Fig. 2. When the signal from a simulated coil drives the input of the integrator, the simulated output shown in Fig. 4 is independent of signal frequency and provides the required flat frequency response for measuring the magnitude of the magnetic field.

One of the major issues with designing an ac integrator is managing the dc offset and output drift. Adding a resistor R_2 in feedback with C_1 , as shown in Fig. 3, eliminates the dc offset problem by bounding the dc gain. The advantage of bounding the dc gain with R_2 is that the amplifier output will not drift into saturation. With the addition of R_2 , the integrator gain is

$1/(j\omega R_1 C_1)$ for frequencies greater than $1/(R_2 C_1)$. The component values for the circuit in Fig. 3 are $R_1 = R_3 = 1.6 \text{ k}\Omega$, $R_2 = 160 \text{ k}\Omega$, and $C_1 = 0.01 \text{ }\mu\text{F}$. The global power supplies for all the circuits are $V_{cc} = +9 \text{ V}$, $V_{ee} = -9 \text{ V}$, and $V_{dd} = +5 \text{ V}$.

The frequency independence of the ac integrator output was verified by running an ac circuit analysis with the output of the ideal coil driving the input of the integrator. The simulation results are shown in Fig. 4, and the integrator output has no frequency dependence over the required frequency range (1–200 kHz). The plot also shows that the frequency response of the integrator circuit in Fig. 3 matches an ideal integrator for the selected BW of the design.

To verify the high-frequency operation of the integrator, a SPICE simulation was performed with a 100-kHz square wave as the input to the integrator. The expected transient response of this standard integrator test is shown in Fig. 5, which is a triangular waveform. The peak of the triangle wave is determined by the gain of the integrator and the input waveform. With an input waveform of $\pm 5 \text{ V}$ and an integrator gain of approximately 0.1 at 100 kHz, the expected peaks of the triangle wave are $\pm 0.5 \text{ V}$, which matches the simulation results.

The signal generated by the coil flows through the rest of the analog front-end stages, as shown in Fig. 2. The output of each stage is calculated by multiplying the output of the previous stage by the gain of the present stage. The calculations for the integrator stage are shown in Table II, which use the coil output voltages in Table I.

B. High-Pass Filter Design

The circuit diagram for the high-pass active filter used in this detector design is shown in Fig. 6. High-frequency inputs greater than the cutoff frequency f_0 emerge from an ideal high-pass filter with unchanged amplitude, whereas those inputs with a frequency less than f_0 are completely attenuated. An active filter eliminates the need for an inductor, which is typically the least ideal circuit element and is bulky, heavy, and expensive.

For high accuracy over a wide frequency range, the frequency response of each filter stage must be flat. Using standard component values and minimizing the part count were important for optimizing the board size and reducing production cost.

The Sallen–Key or voltage-controlled voltage-source (VCVS) quadratic high-pass filter with adjustable dc gain meets all the above requirements. This type of active filter allows f_0 and Q to be easily tuned using standard component values. Keeping Q in the vicinity of one will reduce the effects of component variations on the damping factor, which will minimize overshoots and undershoots. The VCVS high-pass filter also has a Butterworth response, which is very flat in the pass band. Other filters, such as a multiple-feedback filter, are more difficult to tune while maintaining the gain since Q , f_0 , and the gain are dependent on each other.

The circuit analysis for Fig. 6 yields the following result [20]:

$$H(jf/f_0) = \frac{-K(f/f_0)^2}{1 - (f/f_0)^2 + (j/Q)(f/f_0)} = \frac{Vo}{Vi} \quad (6)$$

$$K = 1 + \frac{R_B}{R_A} \quad (7)$$

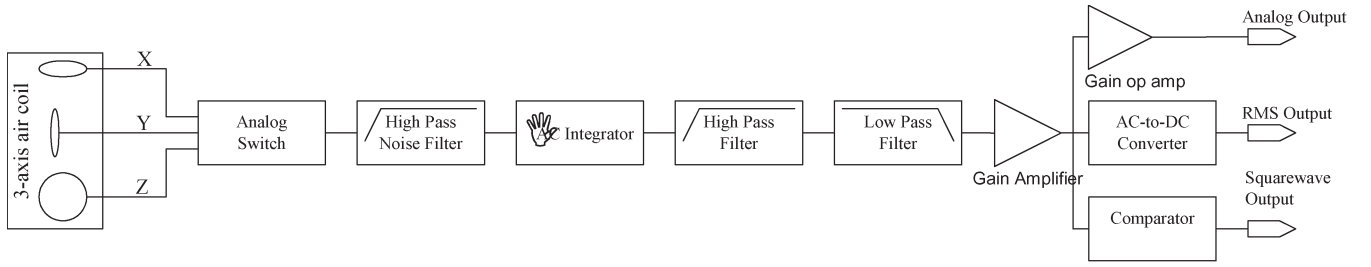


Fig. 2. Block diagram for the analog front-end circuit design.

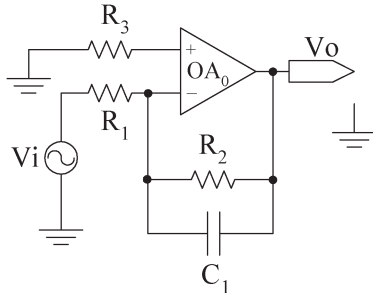


Fig. 3. AC integrator circuit schema.

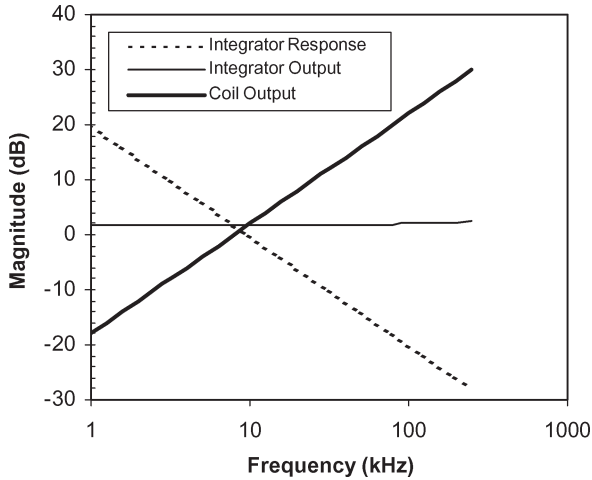


Fig. 4. Frequency response for the ac integrator, coil, and integrator output.

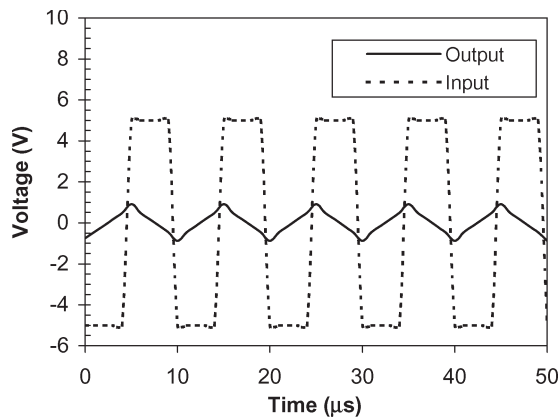


Fig. 5. Integrator response at 100-kHz input frequency.

TABLE II
CALCULATED OUTPUT VOLTAGE AT THE OUTPUT
STAGE OF THE INTEGRATOR

Frequency (Hz)	Magnetic Flux Density (mG)	Coil Output (V)	Integrator Gain (V/V)	Integrator output (V)
1000	0.2	3.00e-06	9.95	2.98e-05
1000	2000	3.00e-02	9.95	3.05e-01
200000	0.2	6.00e-04	0.05	2.98e-05
200000	2000	6.00	0.05	3.05e-01

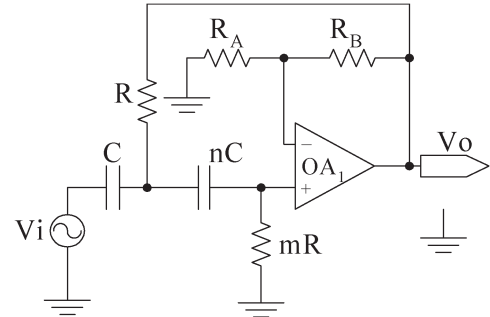


Fig. 6. Second-order high-pass filter circuit.

where K is referred to as a high-frequency gain, and

$$Q = \frac{\sqrt{mn}}{n + 1 + nm(1 - K)}. \quad (8)$$

Q is a damping factor; it can range from 0.5 to 100, with typical values near unity. The values m and n are multipliers for the resistors and capacitors in Fig. 6

$$f_0 = \frac{1}{2\pi RC\sqrt{mn}}. \quad (9)$$

The values of the first RC pair in Fig. 6 in terms of those of the second pair by means of multipliers m and n , respectively, are used to simplify the algebra of the analysis of the transfer function described by (6); in addition, the ratios m and n play an important role in the design procedure for selecting the right values for the components in the filter. The expression for f_0 in (9) depends on R and C , as well as the ratios m and n ; however, Q in (8) depends exclusively on the ratios and gain K , so it can be adjusted without affecting f_0 . Thus, if both f_0 and Q require tuning, we can implement mR and R_B with two variable resistors. First, we adjust mR to achieve the desired

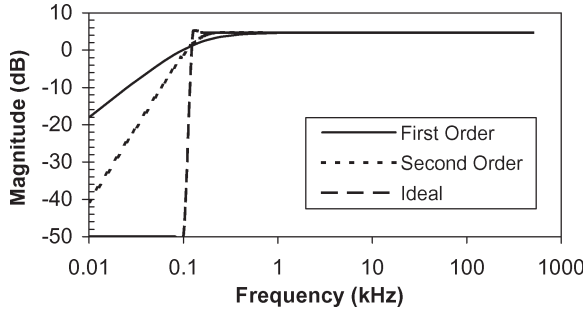
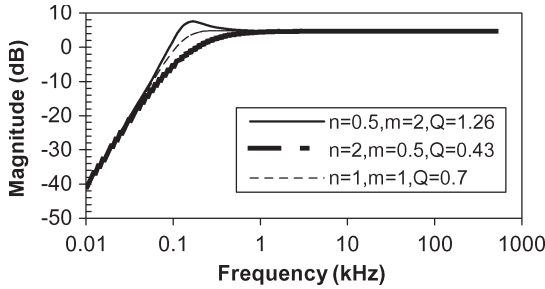


Fig. 7. Ideal, first-, and second-order high-pass filter responses.

Fig. 8. Ideal ($Q = 0.7$), overdamped ($Q = 0.43$), and underdamped ($Q = 1.26$) high-pass filter responses.

f_0 , which also affects Q , and then, we adjust R_B to achieve the desired Q , which does not affect f_0 .

A common task is to find suitable component values that achieve a corner frequency $f_0 = 100$ Hz with a gain of 4.65 dB and a damping factor of $1/\sqrt{2}$. The corner frequency (100 Hz) is intentionally set lower than the desired cutoff frequency (1 kHz) for the wide bandpass filter to avoid the roll off near the corner frequency and keep the frequency response linear. The gain is set based on the system requirement of having a 0–5-V signal driving the ADC. The damping factor was selected to minimize the overshoot and undershoot of the high-pass filter response.

The component values chosen in this design are the following: $C = 47$ nF, $nC = 47$ nF, $R = 34$ k Ω , $mR = 34$ k Ω , $R_A = 14$ k Ω , and $R_B = 10$ k Ω .

The simulation results for the second-order, first-order, and ideal high-pass filters are shown in Fig. 7 with magnitude in decibels versus frequency. Note that the low-frequency asymptotic slope is 40 dB/dec for the second-order filter and 20 dB/dec for the first-order filter. The sharper roll off of the second-order filter is closer to the ideal response, and this produces a more linear response near the cutoff frequency. The frequency response plot for different values of Q is shown in Fig. 8. Note that for low Q values, the transition is very gradual, whereas for high Q values, there is a range of frequencies in the neighborhood of $f_0 = 100$ Hz, where the magnitude is greater than the design goal of 4.65 dB. The borderline between gradual (undershoot) and peaked (overshoot) responses occurs when $Q = 1/\sqrt{2}$. The resulting curve is maximally flat and corresponds to a Butterworth filter response. Above 100 Hz, the response approaches the flat response curve that is required for the desired filter BW.

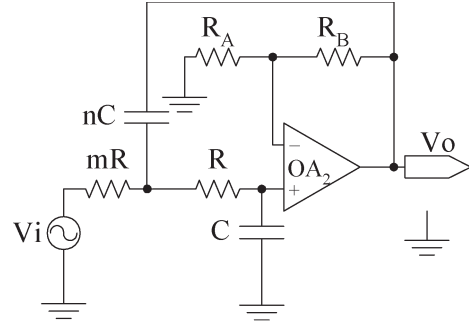


Fig. 9. Second-order low-pass filter circuit design.

C. Low-Pass Filter Design

The circuit diagram for the low-pass active filter drawn in the analog front-end block diagram is shown in Fig. 9. An ideal low-pass filter is characterized by the cutoff frequency f_0 , indicating that the sinusoidal inputs with a frequency less than f_0 go through the filter with unchanged amplitude, whereas those with a frequency greater than f_0 are completely attenuated. The design requirements for the low-pass filter are similar to those of the high-pass filter described in Section IV-B. A VCVS quadratic low-pass active filter circuit with dc gain meets all the performance and cost objectives.

The transfer function for the filter shown in Fig. 9 is given as follows [20]:

$$H(jf/f_0) = \frac{V_o}{V_i} = \frac{K}{1 - (f/f_0)^2 + (j/Q)(f/f_0)} \quad (10)$$

where

$$K = 1 + \frac{R_B}{R_A} \quad (11)$$

$$Q = \frac{\sqrt{mn}}{m + 1 + mn(1 - K)} \quad (12)$$

$$f_0 = \frac{1}{2\pi RC\sqrt{mn}}. \quad (13)$$

For the same reasons that have already been discussed in the high-pass filter section, the ratios m and n in Fig. 9 provide more flexibility for choosing the desired component values of the circuit.

The design requires that suitable component values be identified to obtain the desired values of f_0 , gain, and Q . This design requires $f_0 = 900$ kHz, gain = 8.5 dB, and $Q = 1/\sqrt{2}$.

The component values chosen in this design are the following: $C = 0.01$ nF, $nC = 0.005$ nF, $R = 24.9$ k Ω , $mR = 24.9$ k Ω , $R_B = 20$ k Ω , and $R_A = 12.1$ k Ω .

The simulation results for the second-order, first-order, and ideal low-pass filters are shown in Fig. 10, with magnitude in decibels versus frequency. Note that the high-frequency asymptotic slope is 40 dB/dec for the second-order filter. As discussed in the high-pass filter design section, using the second-order filter results in a more linear response over the operating BW. As shown in Fig. 11, the maximum flat response again corresponds to $Q = 1/\sqrt{2}$. Below 900 kHz, the response approaches the flat response required for the filter.

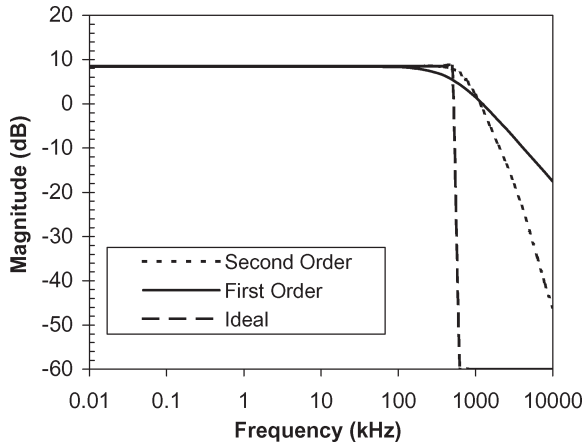


Fig. 10. Ideal, first-order, and second-order low-pass filter responses. Magnitude (in decibels) versus frequency.

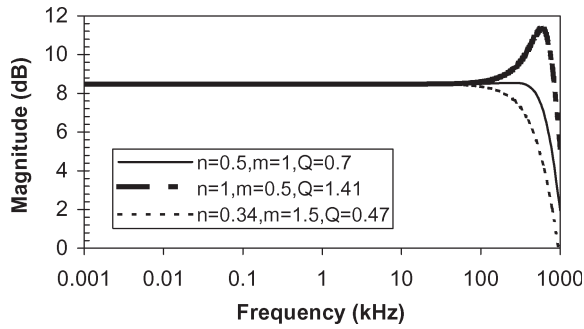


Fig. 11. Ideal ($Q = 0.7$), overdamped ($Q = 0.47$), and underdamped ($Q = 1.41$) low-pass filter responses.

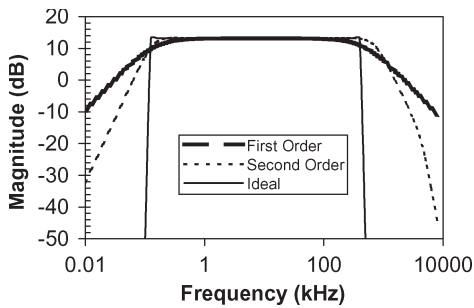


Fig. 12. Ideal, first-, and second-order wide-bandpass filter frequency responses.

The circuits in Figs. 6 and 9 are connected together, yielding a second-order wide bandpass filter with maximum linearity, shown in Fig. 12. This figure also includes the first-order and ideal filter responses for comparison. The flat frequency response with a gain of 13.15 dB over the required BW for this application is critical for accurate measurements through the full frequency range of the meter, as shown in Fig. 13.

The signal generated by the integrator passes through the bandpass filter (combined high-pass and low-pass filters), as shown in Fig. 2. The expected output voltages of the bandpass filter are shown in Table III, which uses the integrator output voltages in Table II.

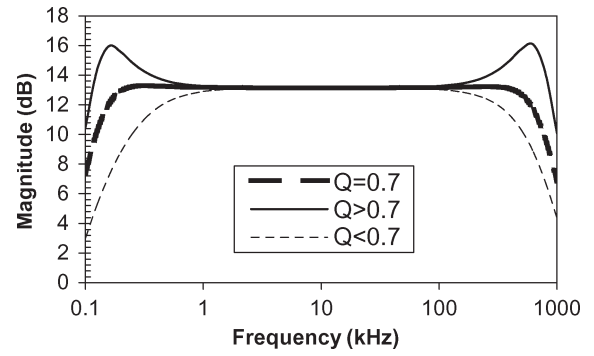


Fig. 13. Ideal ($Q = 0.7$), overdamped ($Q < 0.7$), and underdamped ($Q > 0.7$) wide bandpass filter responses.

TABLE III
EXPECTED OUTPUT VOLTAGES OF THE BANDPASS FILTER
WITH A GAIN OF 13.15 dB

Frequency (Hz)	Magnetic Flux Density (mG)	Integrator Output (V)	Band Pass Filter Output (V)
1000	0.2	2.98e-05	1.36e-04
1000	2000	3.05e-01	1.39
200000	0.2	2.98e-05	1.36e-04
200000	2000	3.05e-01	1.39

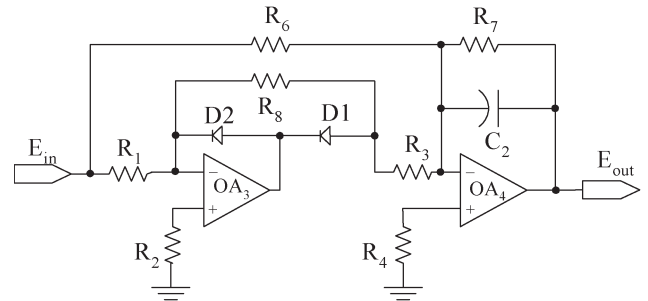


Fig. 14. Precision ac-to-dc converter.

D. AC-to-DC Converter Design

A ripple-free dc signal input is eventually required as the input to the digital portion of this system design; therefore, the (ac) amplified signal is fed through an ac-to-dc converter. The precision ac-to-dc circuit used in this investigation is shown in Fig. 14. Its function with capacitor C_2 removed from the circuit is explained as follows. For negative input signals, the first operational amplifier (op-amp) OA_3 is zero, and no current flows through R_3 . The output of the second op-amp OA_4 is

$$E_{out} = -\frac{R_7}{R_6} E_{in}. \quad (14)$$

For positive input signals

$$E_{out} = R_7 \left[\frac{E_{in}}{R_3} - \frac{E_{in}}{R_6} \right]. \quad (15)$$

If $R_3 = (1/2)R_6$, the output is $(R_7/R_6)E_{in}$; hence, the output is always the absolute value of the input.

Adding capacitor C_2 across R_7 causes op-amp OA_4 to produce an average pure dc output. The filter time constant R_7C_2

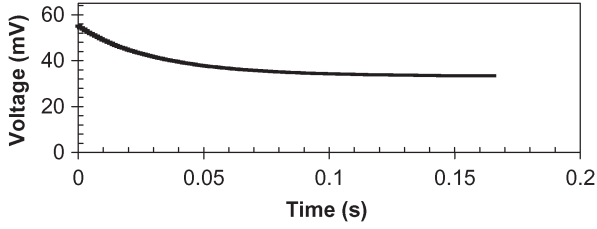


Fig. 15. Signal response of the ac-to-dc RMS converter.

has to be greater than the maximum period of the input signal to have good filtering or averaging without any ripple. In our case, the minimum input frequency of the signal is 1 kHz; then, $T = 1$ ms, and the time constant $R_7C_2 \gg 1$ ms is needed.

The dc output can be adjusted to correspond to either the RMS or the peak of the ac input [21]. For a sinusoidal input $E_{in} = v_i \sin \omega t$, the average dc output is given by

$$E_{out} = \frac{0.64v_i R_7}{R_6}. \quad (16)$$

The selected value for R_7 for RMS calibration is equal to $1.11 R_6$. The component values for the circuit shown in Fig. 14 are $R_1 = 2$ k Ω , $R_2 = 2$ k Ω , $R_3 = 1$ k Ω , $R_4 = 1$ k Ω , $R_6 = 2$ k Ω , $R_7 = 2.2$ k Ω , $R_8 = 2$ k Ω , and $C_2 = 15$ μ F.

For better conversion with less than 1% error, extra care should be taken for frequencies above 125 kHz. During construction, the leads should be kept short, film-type resistor values should be kept low, the power supplies should be bypassed with 0.01- μ F ceramic disc capacitors, the diodes D_1 and D_2 should be reasonably fast, and the amplifiers must have low bias currents. Following these guidelines will reduce the parasitic resistances and capacitances, limit the noise in the system, and keep the nonlinear circuits in a linear region of operation. When combined, these steps result in an operation that is closer to the ideal simulations and allows the components on the circuit board to run at high frequencies with minimal performance degradation.

The simulation output result for a 5-kHz sine-wave input signal with an amplitude of 50 mV is shown in Fig 15. This test shows the importance of adding C_2 across R_7 to act as an active low-pass filter network. This filter eliminates the fluctuations in the rectified voltage and ideally provides a smooth constant-value dc voltage for the input to the ADC. Based on our earlier calculation, the time constant of the ac-to-dc converter was set to 33 ms so that it was much greater than the period of the minimum input frequency (1 ms). Before sampling the signal with the ADC, the output of the ac-to-dc converter must be allowed to settle, for a minimum of five times, the ac-to-dc converter time constant, which is the time needed to fully charge or discharge the capacitor C_2 .

The signal generated by the bandpass filter flows through the variable-gain amplifier and ac-to-dc converter, as shown in Fig. 2. The expected output voltages of the ac-to-dc converter are given in Table IV. The bandpass filter output voltages in Table III are multiplied by 36 or 3.6 for the scale of, respectively, 200 or 2000 mG, which is the combined gain of the ac-to-dc converter and the variable-gain amplifier.

TABLE IV
EXPECTED OUTPUT VOLTAGES FROM THE AC-TO-DC CONVERTER

Frequency (Hz)	Magnetic Flux Density (mG)	Band-Pass Filter Output (V)	AC-to-DC Converter Output (V)
1000	0.2	1.36e-04	5 mV
1000	2000	1.39	5 V
200000	0.2	1.36e-04	5 mV
200000	2000	1.39	5 V

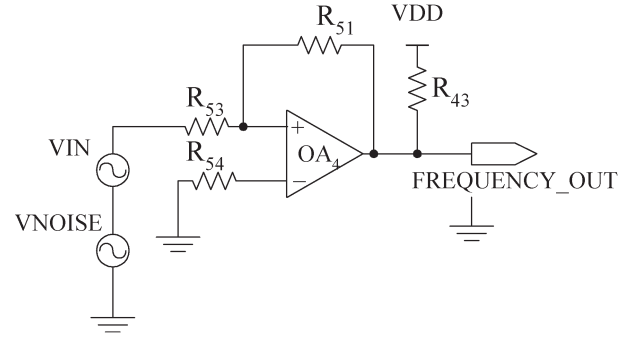


Fig. 16. Comparator with hysteresis circuit design.

The output voltages for each stage of the analog front end are summarized in Table I–IV. Each row in these tables shows the output voltage level when a magnetic field with a known magnitude of either 0.2 or 2000 mG and a frequency of 1 or when 200 kHz is applied to the sensor coil. To match the input requirements of the ADC, the minimum output voltage (ac-to-dc converter output in Table IV) of the analog front end must be 5 mV, which corresponds to a magnetic flux density of 0.2 mG. As shown in the second row of Table IV, the maximum output voltage must be 5 V, which corresponds to a magnetic flux density of 2000 mG. The same process is used to determine the minimum and maximum output voltages at the maximum frequency of 200 kHz. The third and fourth rows of the tables show the detailed calculations for the maximum frequency.

E. Comparator With Hysteresis Design

One of the features for the circuit design is a frequency indicator. Thus, the frequency counter in the microcontroller is used to count the number of digital pulses (0 V or 5 V) per second. The comparator shown in Fig. 2 generates the required digital pulses. The schema of the circuit design using the LM311 comparator is shown in Fig. 16. The component values for the comparator circuit are $R_{43} = R_{53} = R_{54} = 10$ k Ω and $R_{51} = 1$ M Ω .

The comparator looks at the two voltage signals at its input and determines which of the two signals is larger. This function comes in extremely handy in detecting high and low voltage limits for the frequency counter. Because the LM311 output is in the form of an open-collector n-p-n transistor [22], an external pull-up resistor R_{43} is used to drive an output load with a supply voltage (5 V) that is different from the comparator circuit. This characteristic makes LM311 well suited for use with PIC18F452.

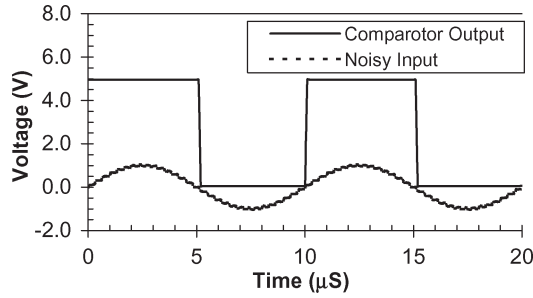


Fig. 17. Comparator response to a noisy input when hysteresis is added.

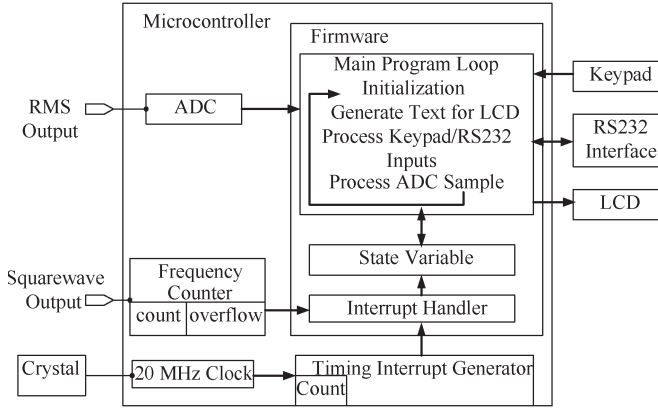


Fig. 18. Block diagram for the circuit digital design.

A feedback resistor was added to the comparator to eliminate output chatter. This problem can show up when the noisy input voltage (V_{IN}) is very close in value to the reference voltage (GND). Under these conditions, the comparator's output may tend to oscillate between states [23]. The effect of the feedback resistor is to make the turn-off level of the comparator somewhat lower than its turn-on level. This significantly reduces the tendency toward "chatter."

The two threshold voltages for the comparator are calculated using the following equations. Equation (17) is for the positive threshold

$$V_{th}^+ = V_3 R_{53} / R_{51} = +5.00 \times 10 / 1000 = 50 \text{ mV} \quad (17)$$

and (18) is for the negative threshold

$$V_{th}^- = -V_3 R_{53} / R_{51} = -50 \text{ mV}. \quad (18)$$

The output goes to the positive state (5 V) when the noisy input signal rises above the positive threshold ($V_{IN} > V_{th}^+$), and the output goes to the negative state (0 V) when the input falls below the negative threshold ($V_{IN} < V_{th}^-$). The simulation results in Fig. 17 show the clean square-wave output voltage response for the comparator, despite the noisy input signals.

V. DIGITAL SIGNAL PROCESSING

An 8-bit microcontroller is used for digital signal processing and to control the interface devices and other digital devices in the meter, as shown in Fig. 18. The RMS output from the analog

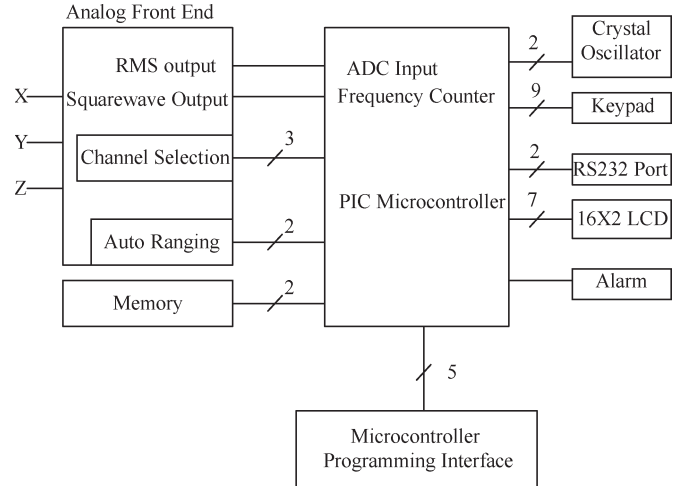


Fig. 19. Top hierarchy model design for the isotropic VLF gaussmeter.

front end is connected to the input of the 10-bit ADC in the microcontroller. The timing interrupt generator and the interrupt handler are configured to sample the ADC every 250 ms.

The sample is then scaled and displayed on the liquid-crystal display (LCD) if the meter is in single-channel mode (x , y , or z). When the meter is in the isotropic mode, the microcontroller stores the sampled data and switches input channels after each ADC reading. Since the channels are sequentially sampled, an isotropic measurement can be calculated and displayed every 750 ms.

The digital output signal from the comparator is connected to a frequency counter in the microcontroller. The frequency counter is based on a dedicated hardware counter [24] that is measured every 1000 ms, and the overflow flag is checked every 13 ms. Both time intervals are controlled by the timing interrupt generator and the interrupt handler.

The data logging feature stores up to 32 000 data samples in a 128-kB external electrically erasable programmable read-only memory. In single-channel mode, only the channel being measured is logged. In isotropic mode, the user can set the meter to store only the isotropic measurement or to store the isotropic measurement along with the x , y , and z readings. The data-logging interval can be set in 1-s increments from 1 s to 2 h or in 1-min increments from 1 min to six days.

Listed below is a summary of the additional external hardware required to build the meter:

- keypad—measured every 13 ms with debounce logic;
- RS232 interface—polled every 13 ms;
- LCD;
- memory;
- alarm.

VI. SYSTEM ARCHITECTURE

The analog front end and the digital components are combined to form the complete measurement system shown in Fig. 19. The analog front end processes the signal from the coil sensor and generates two outputs. The RMS output is connected

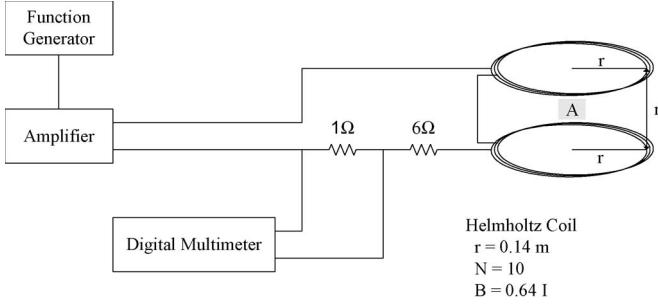


Fig. 20. Helmholtz coil for system-level testing.

to the ADC input for further digital signal processing, whereas the square-wave output is connected to the frequency counter.

The microcontroller controls the channel selection based on input from the user through the keypad or RS232 port. The variable gain amplifier in the analog front end is controlled by the range-selection signals from the microcontroller. The range selection can be set manually, or the microcontroller can dynamically select the range based on the measurements from the coil sensor.

VII. MAGNETIC FIELD METER PERFORMANCE

A. Helmholtz Coil Test Setup

The prototype development and calibration tests for the VLF gaussmeter's field detection circuitry are performed with a Helmholtz coil, which is shown in Fig. 20, that provides a known magnetic flux density as a function of the applied current [25], [26]. It is constructed with two parallel circular coils spaced one radius apart and driven in phase. In our application, the current is adjusted to a value of 150 mA as we sweep the frequencies to maintain a known magnetic field of 100 mG at the center of the coil. The field at the center point A is given by

$$B = \frac{8\mu_0 NI}{5^{3/2}r} = 0.00899 \frac{NI}{r} \quad (19)$$

where B is in gauss, N is the number of turns, I is in amperes, and r is in meters.

The circuitry of the double-sided board used for development and the final verification tests is shown in Figs. 21 and 22. The digital components are on the top half of the board to maximize the separation from the analog components that are on the bottom half. The circuit board is enclosed in a shielded case to reduce the sensitivity to external electromagnetic stray fields. The meter also filters out noise at frequencies outside the desired BW.

B. Mechanical Arrangement of the 3-D Air Coil Sensor

The probe is constructed of three orthogonal nonconcentric air coils aligned so that their axes are mutually perpendicular, as shown in Fig. 23. The radius of each coil is 12.7 mm, and the overall length of the probe is 65 mm.

C. Resonance Frequency Behavior

From an electrical circuit viewpoint, an individual air coil from the probe shown above is primarily an inductor repre-



Fig. 21. Development board—Component side.



Fig. 22. Development board—Solder side.

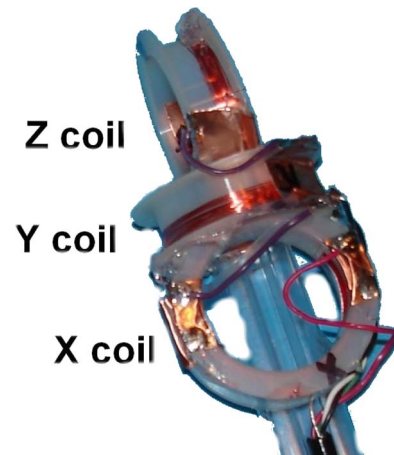


Fig. 23. Construction of a three-axis probe.

sented by the variable L . However, this inductor also contains some parasitic capacitance C and the coil winding resistance R_W . Therefore, the behavior of this coil changes as

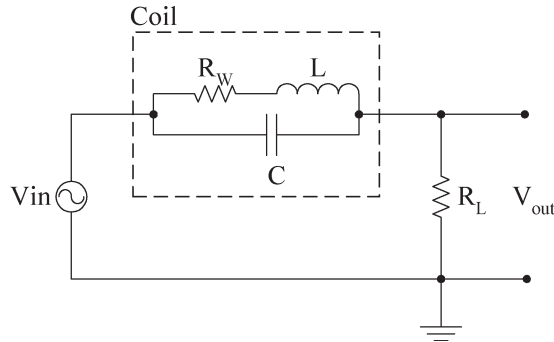


Fig. 24. Parallel resonant band-stop filter.

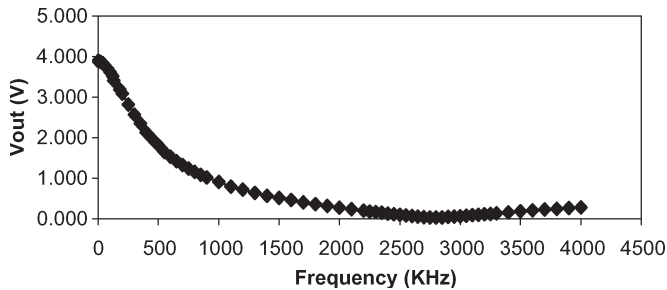
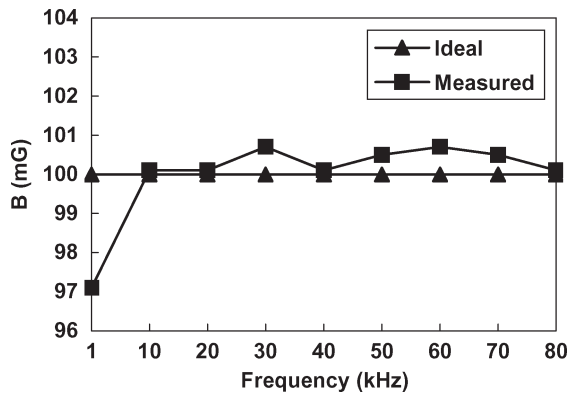
Fig. 25. Band-stop filter response with $f_r = 2800$ kHz.

Fig. 26. Ideal and measured RMS magnetic field responses for the VLF gaussmeter versus frequency.

the frequency of operation is varied. The coil essentially acts as a pure inductor over a fairly wide range of frequencies. At high frequencies, the parasitic capacitance becomes more dominant until the inductor eventually becomes self-resonant. One method for measuring the linear frequency range of the coil is to use a parallel resonant LC band-stop filter [27], as shown in Fig. 24.

The response measured on V_{out} follows the band-stop filter characteristic, as indicated in Fig. 25. When the frequency reaches the resonant value $f_r = 2800$ kHz, the output current is at its minimum, and so is the output voltage V_{out} . It is clear from Fig. 25 that the air coil sensor is operating as a linear inductor over the required BW frequencies.

D. Characterization of the VLF Gaussmeter

The theoretical and experimental results for the linearity of the RMS magnetic field measurement of a sine wave versus frequency are shown in Fig. 26. The field generated by this

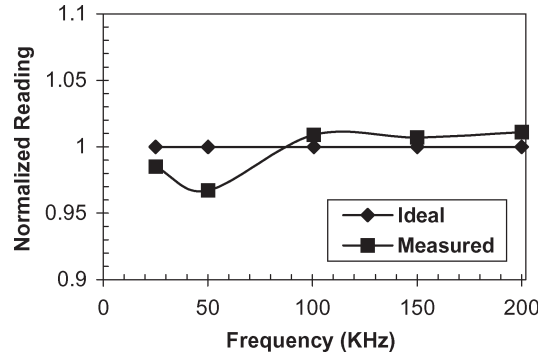


Fig. 27. Linearity response for the VLF gaussmeter frequency behavior.

Helmholtz coil becomes nonlinear above 100 kHz due to the parasitic capacitance between the wire turns. Therefore, tests using this coil were limited to an upper frequency of 80 kHz to avoid this nonlinear region.

The linearity error over the measured frequency range was less than 3% for the worst case. The formula used to calculate this percentage error is given as follows:

$$\%Error = \left(\frac{\text{Measured Field(RMS)} - \text{Actual Field(RMS)}}{\text{Actual Field(RMS)}} \right) * 100. \quad (20)$$

According to the EPA [28], meters with more than 5% error should be considered inaccurate.

A second test was done to study the linearity of the meter over a wider frequency range up to 200 kHz by using a signal generator as the input to the meter. During that test, each time we changed the frequency by a certain ratio, the peak voltage of the signal needed to be adjusted by that same ratio to be consistent with the pickup of the coil. Fig. 27 shows the normalized readings versus the frequencies. The linearity response error over the measured frequency range was less than 3.5%.

The accuracy of low-level field measurements within 10–20 times the meter resolution (0.2 mG) was tested by applying sinusoidal and nonsinusoidal (square and triangle) magnetic fields at a known field strength of 3.9 mG. This magnetic field was generated by using a signal generator to drive a single-turn Helmholtz coil with the same physical dimensions as the coil described in Fig. 20. The single-turn coil eliminates the parasitic capacitances between the wire turns and extends the linear operating frequency of this Helmholtz coil above 200 kHz [25].

The expected data and measured results are shown in Fig. 28 with an overall error of less than $\pm 5\%$ for sine and triangle waves. The first harmonic of the Fourier series for a triangle wave approaches the original waveform. Therefore, the error for the triangle wave is very close to the sine-wave results. The error deviates by more than $\pm 5\%$ for the square wave at frequencies above 100 kHz. This error is mainly caused by the designed upper BW limit of the meter at 200 kHz. Starting at 100 kHz, all the harmonics fall above the upper BW and will be filtered out. This filtering will distort the square wave since a large number of odd harmonics are required to provide a reasonable approximation of the square wave. This distortion will decrease the average result from the ac-to-dc converter.

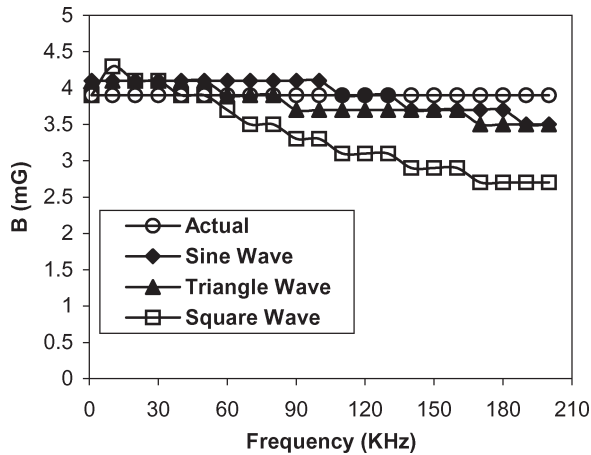


Fig. 28. Applied and measured magnetic field responses for sine, square, and triangle waves at low-level fields.

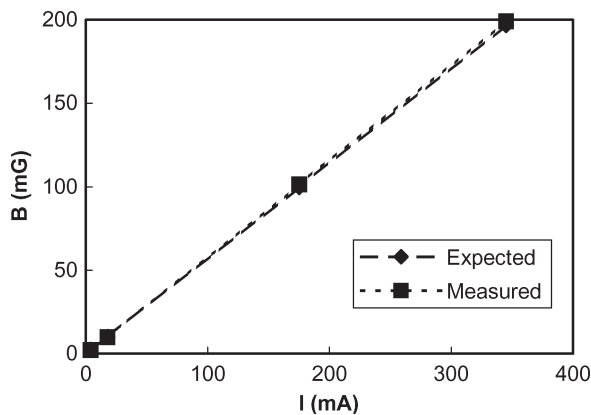


Fig. 29. Applied and measured magnetic field responses versus input current for amplitude linearity at 10 kHz.

The amplitude linearity was tested by placing the probe in known magnetic fields from 2 to 200 mG while holding the frequency stable at 10 kHz. The measured results are shown in Fig. 29.

The response to nonsinusoidal magnetic waveforms generated by the Helmholtz coil was also tested by using an oscilloscope to observe the analog signals. The 12-kHz triangle-waveform input (5 mV/div and 20 μ s/div) from the probe and the resulting analog output (500 mV/div) are shown in Fig. 30. The sharp points of the triangle waveform are rounded off by the limited BW of the meter.

All testing for the prototype development was done at a nominal temperature of 25 $^{\circ}$ C. We expect all the components of the meter to operate from 0 to 50 $^{\circ}$ C, and all the critical gain stages are based on resistor ratios, which should remain constant as temperature varies.

VIII. CONCLUSION

Tradeoffs always exist when an instrument design must be optimized for both high accuracy and high BW (1–200 kHz). The worst-case error for this design is less than 3.5% due to BW limitations of the op-amps. Some error correction could be done within the firmware of the microcontroller. In our case,

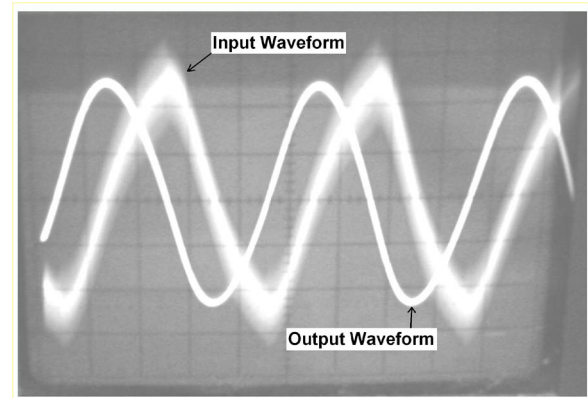


Fig. 30. Noisy input signal from the probe and corresponding analog output from the VLF gaussmeter.

we ran out of internal memory used to store the firmware in the microcontroller due to the multitude of features implemented. Finally, this design can also be done with a proportional frequency response. In this case, the measured magnetic field will be proportional to both the field strength and frequency.

A portable VLF gaussmeter with high resolution (0.2 mG), good linearity, and a wide frequency BW is useful for measuring periodic man-made EMFs in work and home environments. Since this meter is a standalone device with data-logging capabilities, it can be very useful for monitoring remote areas for health and safety concerns. The frequency indicator and the ability to switch between the isotropic mode and the single-axis mode also make it easier to isolate the source of potentially harmful magnetic fields. With all of these features, this instrument is valuable for geologists, volcanologists, climatologists, environmentalists, meteorologists, bioelectromagnetic health researchers, and epidemiologists.

REFERENCES

- [1] R. O. Becker, *Cross Currents*. New York: Penguin Putnam, 1990, pp. 173–304.
- [2] A. S. Safigianni and C. G. Tsompanidou, "Measurements of electric and magnetic fields due to the operation of indoor power distribution substations," *IEEE Trans. Power Del.*, vol. 20, no. 3, pp. 1800–1805, Jul. 2005.
- [3] N. Wertheimer and E. Leeper, "Electrical wiring configurations and childhood cancer," *Am. J. Epidemiol.*, vol. 109, no. 3, pp. 273–284, Mar. 1979.
- [4] C. A. L. Bassett, "Pulsing electromagnetic fields: A new method to modify cell behavior in calcified and noncalcified tissues," *Calcif. Tissue Int.*, vol. 34, no. 1, pp. 1–8, Dec. 1982.
- [5] A. Liboff, "Time-varying magnetic fields: Effect on DNA synthesis," *Science*, vol. 223, no. 4638, pp. 818–820, Feb. 1984.
- [6] A. P. Dubrov, *The Geomagnetic Field and Life: Geomagnetobiology*. New York: Plenum, 1978.
- [7] R. Habash, *Electromagnetic Fields and Radiation: Human Bioeffects and Safety*. New York: Marcel Dekker, 2001, pp. 65–123.
- [8] L. Tomenius, "50-Hz electromagnetic environment and the incidence of childhood tumors in Stockholm county," *Bioelectromagn.*, vol. 7, no. 2, pp. 191–207, Jan. 1986.
- [9] R. J. Spiegel *et al.*, "Measurement of small mechanical vibrations of brain tissue exposed to extremely-low-frequency electric fields," *Bioelectromagn.*, vol. 7, no. 3, pp. 295–306, Jan. 1986.
- [10] N. Wertheimer and E. Leeper, "Possible effects of electric blankets and heated waterbeds on fetal development," *Bioelectromagn.*, vol. 7, no. 1, pp. 13–22, 1986.
- [11] M. E. Herniter, *Schematic Capture With Cadence Pspice*, 2nd ed. Upper Saddle River, NJ: Prentice-Hall, 2003, pp. 54–428.
- [12] B. E. A. Saleh and M. C. Teich, *Fundamentals of Photonics*. New York: Wiley, 1991, pp. 158–165.

- [13] F. S. Barnes, "Mechanisms for electric and magnetic fields effects on biological cells," *IEEE Trans. Magn.*, vol. 41, no. 11, pp. 4219–4224, Nov. 2005.
- [14] C. C. Lo, T. Y. Fujita, A. B. Geyer, and T. S. Tenforde, "A wide range portable 60-HZ magnetic dosimeter with data acquisition capabilities," *IEEE Trans. Nucl. Sci.*, vol. NS-33, no. 1, pp. 643–646, Feb. 1986.
- [15] J. Sedgwick, W. R. Michalson, and R. Ludwig, "Design of a digital Gauss meter for precision magnetic field measurement," *IEEE Trans. Instrum. Meas.*, vol. 47, no. 4, pp. 972–977, Aug. 1998.
- [16] J. L. Guttman, J. Niple, R. Kavet, and G. B. Johnson, "Measurement instrumentation for transient magnetic fields and currents," in *Proc. IEEE Int. Symp. EMC*, Aug. 13–17, 2001, pp. 419–424.
- [17] P. Malcovati and F. Maloberti, "An integrated microsystem for 3-D magnetic field measurements," *IEEE Trans. Instrum. Meas.*, vol. 49, no. 2, pp. 341–345, Apr. 2000.
- [18] M. A. Moresco, W. A. Cronje, and B. M. Steyn, "Modelling and measurement of magnetic fields around a railway track," in *Proc. 7th IEEE AFRICON*, Sep. 15–17, 2004, pp. 749–754.
- [19] R. Stata, "Operational integrators," *Analog Dialogue*, vol. 1, no. 1, Apr. 1967.
- [20] S. Franco, *Design With Operational Amplifiers and Analog Integrated Circuits*. New York: McGraw-Hill, 1988, pp. 96–160.
- [21] D. Wobbschall, *Circuit Design for Electronic Instrumentation*, 2nd ed. New York: McGraw-Hill, 1987, pp. 228–232.
- [22] *Linear Databook*, Nat. Semicond. Corp., Santa Clara, CA, 1982.
- [23] P. E. Allen and D. R. Holberg, *CMOS Analog Circuit Design*. New York: Oxford Univ. Press, 1987, pp. 349–357.
- [24] *Microchip PIC18FXX2 Data Sheet, High Performance, Enhanced Flash Microcontrollers With 10-Bit A/D*, Microchip Technol. Inc., Chandler, AZ, 2002.
- [25] G. Crotti and D. Giordano, "Evaluation of frequency behavior of coils for reference magnetic field generation," *IEEE Trans. Instrum. Meas.*, vol. 54, no. 2, pp. 718–721, Apr. 2005.
- [26] O. Bottauscio, G. Crotti, S. D'Emilio, G. Farina, and A. Mantini, "Generation of reference electric and magnetic fields for calibration of power-frequency field meters," *IEEE Trans. Instrum. Meas.*, vol. 42, no. 2, pp. 549–552, Apr. 1993.
- [27] T. L. Floyd, *Electronics Fundamentals Circuits, Devices, and Applications*, 5th ed. Upper Saddle River, NJ: Prentice-Hall, 2001, pp. 612–631.
- [28] EPA, *Laboratory Testing of Commercially Available Power Frequency Magnetic Field Survey Meter*, pp. 3–4, Jun. 1992.



Saba A. Hanna (M'03) was born in Edde-Batroun, Lebanon, in 1962. He received the B.Sc. and M.Sc. degrees in electrical engineering from the State University of New York at Buffalo in 1987 and 1990, respectively. He is currently working toward the Ph.D. degree in electrical engineering with the Department of Electrical Engineering, University of Vermont, Burlington.

For the past 17 years, he has held different positions. He was a Staff Engineer and a Scientist Developer in analog and digital ASIC design with IBM, Essex Junction, VT, for five years. He founded the Integrity Design and Research Corporation, Essex, VT, in 1991, where he designed numerous devices, mainly ac and dc magnetic field gaussmeters. He is the Senior Engineer and Technical Support Provider for the Integrity Design and Research Corporation's products. He has lectured widely on topics like the biological effects of extremely low frequency (ELF) electromagnetic radiation.



Yuichi Motai (M'01) received the B.Eng. degree in instrumentation engineering from Keio University, Tokyo, Japan, in 1991, the M.Eng. degree in applied systems science from Kyoto University, Kyoto, Japan, in 1993, and the Ph.D. degree in electrical and computer engineering from Purdue University, West Lafayette, IN, in 2002.

He is currently an Assistant Professor of electrical and computer engineering with the Department of Electrical Engineering, University of Vermont, Burlington. His research interests include the broad area of sensory intelligence, particularly of medical imaging, computer vision, sensor-based robotics, and human–computer interaction.



Walter J. Varhue received the B.S. degree in chemical engineering from the University of Connecticut, Storrs, in 1979 and the M.S. and Ph.D. degrees in engineering physics from the University of Virginia, Charlottesville, in 1982 and 1984, respectively.

He is a Professor of electrical engineering with the Department of Electrical Engineering, University of Vermont, Burlington. He conducts research in the area of plasma processing of semiconductor materials and devices.

Stephen Titcomb (M'80–SM'86) received the B.S. degree in physics from Moravian College, Bethlehem, PA, in 1976 and the M.S. and Ph.D. degrees in physics from Lehigh University, Bethlehem, PA, in 1978 and 1983, respectively.

He is currently an Associate Professor of electrical and computer engineering with the Department of Electrical Engineering, University of Vermont, Burlington. His research interests include MOSFET-based biosensors and embedded systems.